Ann. Occup. Hyg., Vol. 57, No. 4, pp. 493–506, 2013

doi:10.1093/annhyg/mes085

Simulation and Evaluation of Respirator Faceseal Leaks Using Computational Fluid Dynamics and Infrared Imaging

ZHIPENG LEI[1], JAMES YANG[1]*, ZIQING ZHUANG[2] and RAYMOND ROBERGE[2]

[1]Department of Mechanical Engineering, Human-Centric Design Research Laboratory, Texas Tech University, Lubbock, TX 79409, USA; [2]National Institute for Occupational Safety and Health, Pittsburgh, PA 15236, USA

Received 9 December 2011; in final form 11 October 2012; Advance Access publication 13 December 2012

This paper presents a computational fluid dynamics (CFD) simulation approach for the prediction of leakage between an N95 filtering facepiece respirator (FFR) and a headform and an infrared camera (IRC) method for validating the CFD approach. The CFD method was used to calculate leak location(s) and 'filter-to-faceseal leakage' (FTFL) ratio for 10 headforms and 6 FFRs.The computational geometry and leak gaps were determined from analysis of the contact simulation results between each headform-N95 FFR combination. The volumetric mesh was formed using a mesh generation method developed by the authors. The breathing cycle was described as a time-dependent profile of the air velocity through the nostril. Breathing air passes through both the FFR filter medium and the leak gaps. These leak gaps are the areas failing to achieve a seal around the circumference of the FFR. The CFD approach was validated by comparing facial temperatures and leak sites from IRC measurements with eight human subjects. Most leaks appear at the regions of the nose (40%) and right (26%) and left cheek (26%) sites. The results also showed that, with N95 FFR (no exhalation valves) use, there was an increase in the skin temperature at the region near the lip, which may be related to thermal discomfort. The breathing velocity and the viscous resistance coefficient of the FFR filter medium directly impacted the FTFL ratio, while the freestream flow did not show any impact on the FTFL ratio. The proposed CFD approach is a promising alternative method to study FFR leakage if limitations can be overcome.

Keywords: computational fluid dynamics; infrared image; leak; respirator; respirator fit

INTRODUCTION

The N95 filtering facepiece respirator (FFR) is widely used in workplace environments to prevent exposure to hazardous aerosols. The protection provided by an FFR is a function of leakage between the respirator and the face (Liu *et al.,* 1993) as well as particle penetration through the filter medium (Grinshpun *et al.,* 2009). Quantitative fit tests can determine the overall performance of a respirator but cannot identify the specific location of facepiece leaks. The goal of this project was to develop and evaluate a method for detecting and predicting the most likely leak locations for N95 FFRs.

By measuring heat convection of exhaled air on facial skin, an infrared camera (IRC) can be used to measure FFR facepiece leakage by capturing temperature changes of the human face region bordering the FFR (Roberge *et al.,* 2011). Several methods have been used in the past to locate respirator

---

*Author to whom correspondence should be addressed.
Tel: 806-742-3563 (extension 229); fax: 806-742-3540;
e-mail: james.yang@ttu.edu

facepiece leak locations. Oestenstad *et al.* (1990, 2010) used facial deposition of a fluorescent tracer and black light visualization to photograph leak location and shape on subjects wearing half-mask respirators. They found that facial dimensions were significantly associated with leak location, while gender and respirator size showed a weaker association. Crutchfield and Park (1997) conducted a study assessing quantitative fit test systems and observed that leak locations had a significant effect on leakage measurements. Lee *et al.* (2005) studied the impact of inhalation flow rates and leak sites on performance of N95 FFRs, and they noted that during inhalation, the protection factor was higher when leaks occurred at the nose than at the cheek and chin.

An alternative approach to study the air flow is a computational fluid dynamics (CFD) method that uses numerical methods and algorithms to solve fluid problems and gain information about velocity, pressure, and temperature (Chung, 2001). In previous studies, the air flow around a headform or a whole human body has been simulated by the CFD method (Anthony and Flynn, 2006; Craven and Settles, 2006), following a four-step procedure: (i) the surface geometry of a manikin or a headform is captured by a 3D scanner; (ii) the computational domain is divided into two regions, namely an inner domain that surrounds the geometry of the headform or the human body meshed into small size grids and an outer domain that contains the environmental space meshed into structured grids (Sorensen and Voigt, 2003); (iii) ventilation, including exhalation and inhalation, is incorporated into the simulation (Gao and Niu, 2004) ; and (iv) air flow and heat transfer are calculated. However, these models did not contain the clothing, FFR, helmet, and glasses commonly worn in hazardous workplaces.

Faceseal leakage of an FFR can be significantly impacted by facial dimensions, breathing intensity, and activity (Han and Lee, 2005 ; Lee *et al.,* 2005; Grinshpun *et al.,* 2009; Oestenstad *et al.,* 1990, 2010). Facial features affect the flow field near the nose or mouth of a breathing human (Anthony *et al.,* 2005). A combination of an FFR and a headform in a CFD simulation is necessary for estimating potential leaks. However, creating a human-like facial seal of a protective facemask with a headform is difficult (Butler, 2008). One ongoing issue is that the CFD method does not allow facemask/human face deformation and therefore may result in an inadequate facial seal. Previously, Lei *et al.* (2010, 2011) studied the contact of N95 FFRs and five sizes of headforms using the finite element (FE) method. Although the main purpose of these studies was to determine contact pressure, the investigators successfully generated deformed shapes and fitting positions of FFR and headform models that offer a geometrical basis for CFD simulations of FFR facepiece leakage.

The ultimate goal of this study was to develop a tool for N95 FFR designers and regulators to conveniently examine and evaluate the fit and comfort of an N95 FFR on headforms that represent the range of US respirator users. To achieve this goal, the basic N95 FFR leak characteristics and factors that can affect facepiece leakage need to be elucidated. As a pilot investigation, this study determined leak location(s) and air flow rates through two pathways (FFR filter medium penetration and faceseal leakage) when an N95 FFR was virtually donned by a headform in a CFD simulation model. Results can be used to identify common leak locations and predict the protection factor for different combinations of facial characteristics and air flow.

This study developed a method for studying the inner flow within the volume (FFR deadspace) formed between the FFR and the headform surface, in addition to the flow outside of the FFR based on previous contact simulation work (Lei *et al.,* 2011). Air flow and heat transfer over the human face were simulated by the CFD method. An algorithm to generate the meshed flow field for the CFD simulation was developed. Time-dependent facial temperature contours were computed for determining leak locations. Facial temperatures and leak locations from experiments and simulations were compared for validation.

METHODS

Digital models

In 2003, the National Institute for Occupational Safety and Health (NIOSH) conducted an anthropometric survey of 3997 US civilian workers and developed new respirator fit test panels including a bivariate panel and a principal component analysis (PCA) panel (Zhuang and Bradtmiller, 2005; Zhuang *et al.,* 2007). The PCA panel was then used to classify subjects into five size categories—large, medium, small, long/narrow, and short/wide—and develop five representative headforms for each category (Zhuang *et al.,* 2010).

Digital models of six N95 FFRs (3M 1860: medium/large; 3M 1860s: small; Moldex 2200: medium/large; Moldex 2201: small; 3M 8210: medium/large; and 3M 8110s: small) were scanned using a 3D imaging system. We assumed no shape variation between an experimental FFR and its digital model. During post-processing, asymmetry of each N95 FFR digital model was reduced.

Contact simulation

Ten FE headforms (Table 1) were constructed from their digital models using the method developed by Lei *et al.* (2010). Each headform model consisted of six regions: forehead, left cheek, right cheek, chin, neck, and back of the head. Facial and jugular regions have multilayer structures in which the skin layer is at the headform surface and the bone layer is at the innermost level of the headform (De Greef *et al.,* 2006; Lei *et al.,* 2011).

The simulation process mirrored the procedures for donning a respirator: the top strap is first pulled over the head and placed at the top of the back of the head (occiput) above the ears, after which the bottom strap is pulled over the head and positioned around the neck below the ears. The wearer then adjusts the pliable nose clip. Contact occurs between the facepiece and the face as well as between the straps and the head. Note that the advantage of the FE contact simulation model (Lei *et al.,* 2011) is that the magnitude and direction of strap forces are automatically determined.

The six FE FFR models were constructed of multiple layers and two straps, following the design of the original respirators. Multiple layers were made using scanned data, and two straps were made using measurements of strap length and width. An adjustable plastic nose clip was included in the FFR models for the 3M 1860, 3M 1860s, 3M 8210, and 3M 8110s respirators.

The contact simulation process consisted of three steps: (i) pulling the straps around the back of the headform and holding the FFR to the front of the human face and leaving a gap between the FFR and human face, (ii) adjusting the straps to the FFR and releasing the FFR so that it moves toward the face, and if appropriate, (iii) deforming the nose clip for molding the nose area to the nasal bridge [see Lei *et al.* (2011) for more details]. In its final state, the respirator contacts the face, and the relative position between the respirator and the face remains fixed.

CFD simulation

Coupling of air flow and heat convection around the face of the headform was solved to detect facepiece leakage using CFD software (ANSYS FLUENT 12.0, Canonsburg, PA, USA). An adequate fit was defined by the condition that almost all exhaling and inhaling air passes through the filter medium. Leakage occurs if air passes through leak(s) between the face and the respirator surface border. Prior to simulation, the calculation domain must be determined. During exhalation, breathing air

Table 1. Facial dimensions of 10 digital headforms.

Headform	1	2	3	4	5	6	7	8	9	10
Face width (mm)	131	126	139	140	147	145	130	132	136	133
Face length (mm)	111	115	117	114	114	108	126	120	125	120
NIOSH bivariate panel size	3	3	4	4	5	5	6	6	7	7
Forehead										
Skin (mm)	4.2	4.2	4.2	4.2	5	5	5.4	5.4	5.4	5.4
Bone (mm)	2.5	2.5	2.5	2.5	2.5	2.5	2.5	2.5	2.5	2.5
Left/right										
Skin (mm)	2	2	4	4	4	4	3	3	3	3
Cheek										
Muscle (mm)	4.5	4.5	5.5	5.5	5.5	5.5	5	5	5	5
Fat (mm)	7.5	7.5	8.5	8.5	8.5	8.5	8	8	8	8
Bone (mm)	2.5	2.5	2.5	2.5	2.5	2.5	2.5	2.5	2.5	2.5
Chin										
Skin (mm)	3	3	3	3	3	3	3	3	3	3
Muscle (mm)	4	4	4	4	5	5	6	6	6	6
Bone (mm)	2.5	2.5	2.5	2.5	2.5	2.5	2.5	2.5	2.5	2.5
Neck										
Skin (mm)	3	3	3	3	3	3	3	3	3	3
Muscle (mm)	10	10	10	10	12	12	12	12	12	12
Bone (mm)	2.5	2.5	2.5	2.5	2.5	2.5	2.5	2.5	2.5	2.5

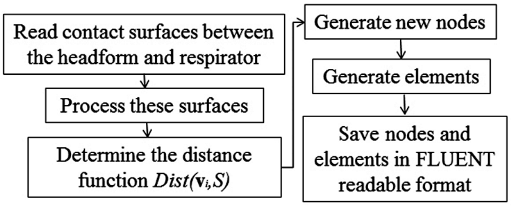

Fig. 1. Flowchart for generating mesh for CFD simulation.

exits the nostrils and enters the deadspace bounded by the respirator's innermost surface where it partly contacts the face. During inhalation, deadspace air enters the nostrils, producing a negative pressure field that drives air movement from the outside to the interior of the respirator facepiece. Thus, the air flow field includes three zones: between the headform and the respirator, inside the filter medium, and external to the respirator. The CFD simulation method thus consists of four components: generating the meshed zones of the air flow field, defining the mathematical model of flow and heat transfer, selecting suitable solvers, and calculating temperature, pressure, and velocity fields.

The mathematical description of air flow field geometry includes a set of discretized elements (Chung, 2001). A MatLab (MathWorks, Natick, MA, USA) program was developed for meshing the air flow field (Fig. 1) using six steps:

(1) Input the contacting surfaces of the headform and respirator. The geometries of these two surfaces were described mathematically as nodes and triangles. Each node was denoted by a unique number and its global Cartesian coordinates, and each triangle was defined by the numbers of three nodes. Figure 2a shows the inner surface of the FFR and the outer surface of the headform that were extracted from the final state of the contact simulation.

(2) Process the surfaces. The respirator and headform surfaces were placed in the same global coordinate system, in which the z_0-coordinate is in the direction normal to the headform frontal face, the x_0-coordinate is along the lateral direction of the headform, and the y_0-coordinate is along the vertical direction of the headform. The origin of the global coordinate system is located on the intersection point of three perpendicular planes (the sagittal plane, coronal plane, and transverse plane that pass through the nose tip point), and the x_0-, y_0-, and z_0-axes are parallel to the intersection lines of these planes. Because only cheek, nose, chin, and neck areas of the headform interacted with the FFR, the headform surface was trimmed for computational efficiency (Fig. 2b). These two surfaces were rotated -20° around the x_0-axis to guarantee that none of the triangles had a norm approximately perpendicular to the z axial direction. After rotation, a new coordinate system (xyz) was generated for later meshing processes and CFD simulations, where x overlaps with x_0, y is in a vertical direction and pointed up, and z is perpendicular to both x and y with right-hand rule.

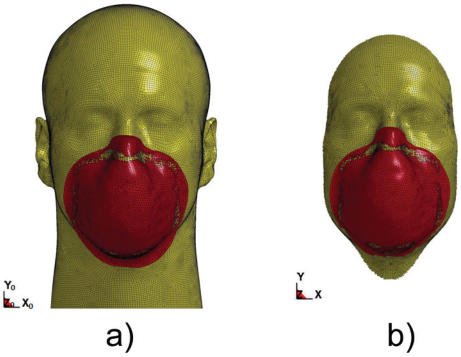

Fig. 2. (a) The inner surface of the respirator and the outer surface of the headform; (b) the inner surface of the respirator and the trimmed surface of the headform.

(3) Calculate the distance function that mathematically represents the geometrical interaction between the headform surface and the respirator surface. Both surfaces were projected along the z axial direction to the oxy plane in order to obtain Segment K that contains the union of these two projection areas on the oxy plane. Segment K was discretized into nodes and rectangular grids. Then, by projecting every node of Segment K along the z axial direction to the headform and FFR surfaces and introducing the distance function $\mathrm{Dist}(\mathbf{v}_i, S)$, where $\mathbf{v}_i$ was the position vector of Node i of the oxy plane and Surface S was either the respirator surface or the headform surface, the projecting distance was calculated between every node of Segment K and either the FFR or headform surface. The detailed definition of $\mathrm{Dist}(\mathbf{v}_i, S)$ and the approaches to obtain it are presented in Appendix 1.

(4) Generate new nodes, which fully distribute the air flow fields by translating every node of Segment K along the z axial direction 26 times. The distance function was used to calculate the transitional distance and determine to which zone the new nodes belong.

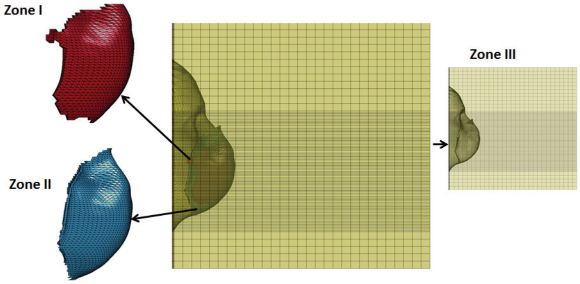

Fig. 3. Mesh generation in Zone I (the volume between the headform and the inner surface of the respirator), Zone II (inside the respirator's medium), and Zone III (outside of the respirator).

(5) Generate elements in the three zones that include (a) the volume between the headform and the respirator (Zone I), (b) the filter medium (Zone II), and (c) the region outside of the respirator (Zone III). A mesh was created by adding one layer at a time.

(6) Save the results in a format that ANSYS FLUENT software can read.

The geometry was successfully meshed into three zones as shown in Fig. 3. The dimension of the whole meshed domain in the z axial direction was 350 mm. Zone I consisted of five layers of elements, which had the same thickness at the arbitrary location with the same x- and y-coordinates. Zone II was modeled as a porous media and had one layer of elements with a uniform thickness of 4 mm, the thickness of the FFR filter medium. Zone III had a structure of 35 layers with 6 boundary layers and a structure of 29 layers without 6 boundary layers. The six boundary layers had the thickness of 0.5 mm, and other layers in Zone III had a thickness of 10–12 mm. The dimensions and mesh element sizes in the x and y axial directions were controlled by Segment *K* in the xy plane. We chose Segment *K* as a rectangle with a width of 330 mm in the x axial direction and a height of 334 mm in the y axial direction. In the middle area of Segment *K,* where the nodes could be projected on the FFR surface along the z axial direction, the mesh element size is 2 mm, while in the other area of Segment *K*, the mesh element size is 10 mm.

The mathematical model included flow zone properties, boundary conditions, and initial conditions. The air flow inside the respirator deadspace and environment (Zones I and III) was an unsteady incompressible flow and heat convection problem. The thermal effects of radiation and evaporation were ignored. The governing equations for Zone I and III were the mass conservation equation, the three-dimensional Reynolds-averaged Navier–Stokes equations, and the energy equation (see Pope, 2000 for details). The Renormalization Group (RNG) $k-\varepsilon$ turbulence model was used because it has been proven as an accurate predictor in indoor air simulations (Posner *et al.,* 2003). The description and the suggested constants of the RNG $k-\varepsilon$ turbulence model were given by Yakhot and Orzag (1986). Consistent with its FE model, the human face has skin, fat, muscle, and bone. However, in this CFD simulation, the face was constructed as a shell with segments of the forehead, cheek, and chin. The Pennes equation (Pennes, 1948) was used to model the heat conduction of the face:

$$\rho_f c_f \frac{\partial T_f}{\partial t} = k_f \nabla^2 T_f + \rho_b w_b c_b (T_b - T_f), \qquad (1)$$

where T_f, ρ_f, c_f, and k_f are the temperature, density, specific heat, and conductivity of the human face, and ρ_b, w_b, c_b, and T_b are the density, perfusion, specific heat, and temperature of the human blood in the facial area. These parameters of the face shell were all calculated by summing the weighted parameters of skin, fat, muscle, and bone under the facial area. The basic parameters of facial tissues came from the UTCI-Fiala model (Fiala *et al.,* 2012), and the weights were based on the tissue thicknesses shown in Table 1.

The filter medium (Zone II), made up of randomly oriented fibers, was defined as a porous media to simulate its resistance to flow. In laminar flow through porous media, the pressure drop is proportional to velocity, and the momentum equation is replaced by Darcy's law:

$$\nabla p_a = -\frac{\mu_a}{\alpha} \mathbf{V}_a, \qquad (2)$$

Table 2. Summary of parameters.

Parameter	Unit	Value	Source
Air density ρ_a	kg / m^3	1.225	
Air-specific heat c_a	j/(kg•K)	1006.43	
Air thermal conductivity k_a	w / (m•K)	0.0242	
Air viscosity μ_a	kg / (m•s)	1.789×10^{-5}	
FFR density ρ_f	kg / m^3	910	Li *et al.*, 2006
FFR-specific heat c_f	j / (kg•K)	1715	Li *et al.*, 2006
FFR thermal conductivity k_f	w / (m•K)	0.05	Li *et al.*, 2006
FFR viscous resistance coefficient $1/\alpha$	1 / m^2	1.12×10^{10}	Li *et al.*, 2006
FFR porosity ε		0.88	Gao *et al.*, 2011
Facial layer density ρ_s	kg / m^3	1026–1218	Fiala *et al.*, 2012
Facial layer-specific heat c_s	j / (kg•K)	3135–3735	Fiala *et al.*, 2012
Facial layer thermal conductivity k_s	w / (m•K)	0.39–0.65	Fiala *et al.*, 2012
Blood perfusion rate w_b	l/(s•m^3)	1.5–8.2	Fiala *et al.*, 2012
Blood density ρ_b	kg / m^3	1100	Ng *et al.*, 2010
Blood-specific heat c_b	j / (kg•K)	3300	Ng *et al.*, 2010
Blood temperature T_b (=core temperature)	K	309.6	

where $1/\alpha$ is the viscous resistance coefficient (ANSYS, 2009). A viscous resistance coefficient, $1/\alpha = 1.12 \times 10^{10} (\mathrm{m}^{-2})$, was adopted for the FFR filter medium, based on experiments quantifying the air permeability of N95 FFRs (Li *et al.*, 2006). An effective conductivity in the filter medium was used in the heat conduction equation:

$$\frac{\partial}{\partial t}[(1-\varepsilon)\rho_f c_f T_a + \varepsilon \rho_a c_a T_a] + \rho_a \nabla \bullet (\mathbf{V}_a T_a) = \nabla \bullet \{[(1-\varepsilon)k_f + \varepsilon k_a] \nabla T_a\} \quad (3)$$

where ε, ρ_f, c_f, and k_f are the porosity, density, specific heat, and thermal conductivity of the filter medium. Table 2 gives a summary of parameters used for defining the mathematical model.

The external surfaces of the entire computational domain were defined with seven boundaries: forehead, cheek, nostril, chin, and exterior I–III (Fig. 4). Because our problem mainly considered normal breathing with a low respiratory flow rate, we assumed that expiration and inhalation in this study were purely nasal breathing, although it is recognized that use of a respirator causes many users to switch from nasal to oral breathing (Harber *et al.*, 1997). The nasal tunnel was considered as a cuboid, and the cross sectional area is about 1 cm^2, consistent with the measurements from Gupta *et al.* (2010). The periodic change of exhalation and inhalation was described by an unsteady air velocity or air flow rate (Hyun and Kleinstreuer, 2001; Hayashi *et al.*, 2002; Sorensen and Voigt, 2003). Ventilation was taken into account by giving the nostril a prescribed velocity profile. As shown in Fig. 5, we defined a time-dependent velocity profile as proposed by Russo and Khalifa (2011). The profile is piecewise linear, and the exhalation duration (3 s) is longer than the inhalation duration (1.75 s). The fact that the exhalation has a longer duration than

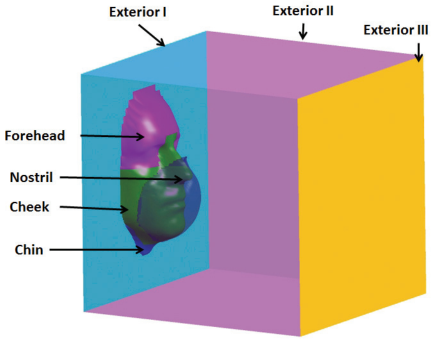

Fig. 4. Boundary surfaces: forehead, nostril, cheek, chin, and exterior I–III.

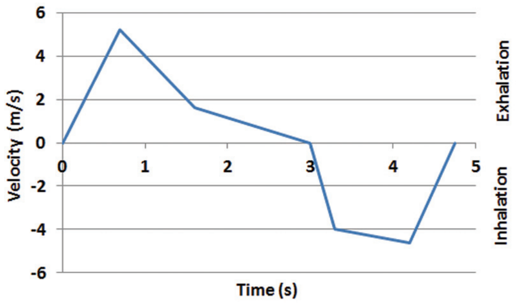

Fig. 5. The profile of respiratory flow rate (m/s) for the normal breathing pattern measured by Russo and Khalifa (2011).

Table 3. Boundary and initial conditions.

Nostril	Velocity inlet: Velocity profile as Fig. 6, direction normal to the boundary, temperature 307.6 K, turbulent intensity 1%, and hydraulic diameter 10 mm.
Forehead	Wall: No slip; shell conduction, thickness 11.2–12.4 mm, inner side temperature 309.6 K, heat generation $\rho_b w_b c_b (T_b - T_s)$.
Cheek	Wall: No slip; shell conduction, thickness 21–25 mm, inner side temperature 309.6 K, heat generation $\rho_b w_b c_b (T_b - T_s)$.
Chin	Wall: No slip; shell conduction, thickness 14–16 mm, inner side temperature 309.6 K, heat generation $\rho_b w_b c_b (T_b - T_s)$.
Exterior I	Pressure outlet: Gauge pressure 0 Pa, backflow temperature 296.6 K, turbulent intensity 1%, length scale 100 mm.
Exterior II	Pressure outlet: gauge pressure 0 Pa, backflow temperature 296.6 K, turbulent intensity 1%, length scale 100 mm.
Exterior III	Wall: Slip, temperature 296.6 K.
Initial condition	Velocity is zero; temperature is 296.6 K; turbulent kinetic energy is 10^{-5} m^2/s^2 ; turbulent dissipation rate 10^{-6} m^2/s^3 .

the inhalation has been well recognized, although Grinshpun *et al.* (2009) and Gupta *et al.* (2010) reported that the breathing pattern in respirator fit tests can be well approximated by a sinusoidal function. Consequently, the average respiratory rate was 12–13 breaths per minute, and the minute volume was about 7.57 l. The peak exhalation flow rate was 31 l/min, and the peak flow rate was 27.6 l/min. The air flow temperature T was set as 307.6 K (Dubrowski, 1975; Jones, 1982). The Reynolds number calculated at the leaking gap was 3559 with the highest breathing velocity 5.2 m/s.

We assumed no head movement or no respirator deformation during the CFD simulation. The boundaries of the forehead, cheek, and chin were defined as thin walls. Different thicknesses were assigned to the three facial boundaries according to the facial soft tissue thicknesses in Table 1. The outer side of the wall, which is adjacent to the air flow and the respirator, had a zero velocity in all directions, and the inner side of the wall, which is the core of the human body, had a fixed core temperature T of 309.6 K, similar to the oral temperature (309.38–309.88 K) measured by Roberge *et al.* (2011). Heat exchanging from blood flow within the facial layer was considered by introducing a heat generation term: $\rho_b w_b c_b (T_b - T_s)$.

The surfaces of exterior I and II are around the human face, and the surface of exterior III is 350 mm away from the human face as shown in Fig. 4. Boundary surfaces of exterior I and II used the pressure outlet boundary condition defined in the ANSYS software. The pressure at the exterior of Zones I and II is fixed and equal to standard atmospheric pressure (0 Pa). Because part of exterior I is near the forehead, cheek, and chin during the inhalation process, there will be backward flow entering Zone III through exterior Zones I and II. The temperature of back flow passing through exterior Zones I and II was 296.6 K, room temperature measured by Roberge *et al.* (2011). Because exterior Zone III had a relatively long distance to the human face (approximately 350 mm), we assumed that no air flow through exterior Zone III, and a wall boundary condition with a fixed temperature of 296.6 K was assigned to exterior Zone III. The fixed temperature on exterior Zone III was essential to the energy equilibrium of the system. At the initial time, velocities in all three directions were zero, and temperature was 296.6 K. Table 3 provides the detailed definition of boundary conditions and initial conditions.

The finite volume method was used to solve air flow, the basic idea of which is to divide the computational domain into a large number of control volumes and to build an algebraic system for the control volumes (Chung, 2001). The algorithm named Semi-Implicit Method for Pressure-Linked Equation, which is based on the predictor–corrector approach, was selected for pressure–velocity coupling. The spatial discretizations of the momentum, turbulent kinetic energy, turbulent dissipation rate, and energy used the second-order upwind method, while the pressure used the PRESTO! (PREssure Staggering Option) scheme. Transient formulation was first-order implicit. The simulation process was divided into two sequential stages.

Stage I was a steady simulation without a breathing process. Heat transfer in the skin, respirator dead space, filter medium, and environment was purely by conduction. Because temperatures at the inner side of boundaries of the forehead, cheek, and chin are higher than the initial temperature (room temperature), the temperature field in the whole domain slowly increases until reaching a steady state. In ANSYS FLUENT software, the energy residual was 5×10^{-8} after about 12 000 iterations.

Stage II was a transient simulation with a breathing process. Because the air flow began to pass through the nostril, heat convection occurred between breathing air and the face and between breathing air and the filter media. ANSYS FLUENT software calculated the velocity, temperature, pressure, turbulent kinetic energy, and turbulent dissipation rate fields. For every headform-N95 FFR combination, a duration of three respiratory cycles (about 14.25 s) was simulated. In every time step, the residuals of variables converged with different speeds and the continuity residual usually had the slowest convergence rate. We set the lower bound of the continuity residual as the iteration stopping criterion. A time step of 0.05 s and the continuity residual's lower bound 1×10^{-4} for iteration stopping criterion were used in all simulations. The grid independency, iteration errors, and time step errors are discussed in Appendix 2.

Because heat convection occurs between breathing air and the face, the air flow pattern can be observed by monitoring temperature distribution on the face. Because the critical regions of the face impacted by leakage occur at the respirator border, we defined four anatomical sites (area A: nasal region; area B: right cheek region; area C: left cheek region; area D: chin region), similar to those used by Oestenstad *et al.* (2010) (Fig. 6). One method for determining faceseal leakage is to record temperature contours on each of the four anatomical areas during Stage II of the CFD simulation. Within one breathing cycle, faceseal leakage can be identified by an increase or decrease in temperature at any of the four anatomical sites.

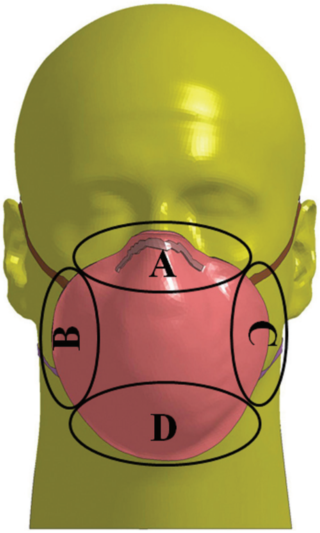

Fig. 6. Four anatomical sites of the human face on the FFR border.

Using infrared images of respirator leakage to validate simulation results

From earlier studies, 48 thermal video images were obtained from IRC recordings of 8 subjects performing quantitative fit tests wearing the same N95 FFRs used in this study (Roberge *et al.*, 2011; Viscusi *et al.*, 2011). The facial dimensions of the eight subjects were measured and classified as five different head sizes according to the NIOSH bivariate panel (Zhuang *et al.*, 2007). Thermal images were recorded by a Model SC 5600-M High Resolution Cooled IRC (FLIR System, Inc., North Billerica, MA, USA) operated in the 3–5 μm spectral range with an accuracy of ±1% K. Images were post-processed over a narrow temperature range (1.5 K) to capture very small temperature changes. The IRC was positioned directly in front of the subjects, who stood throughout the FFR fit test at a distance of 1 m against a dark background. Head movement was minimized. Leaks were identified during one breathing cycle when a change in skin temperature was observed in the region of the face bordering the respirator.

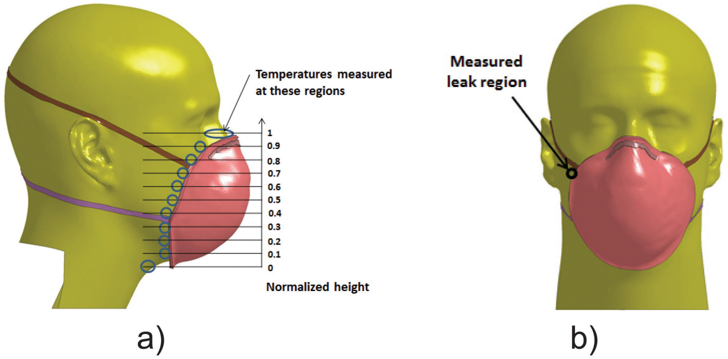

Fig. 7. Regions used for temperature validation: (a) Eleven anatomical regions near the border of the filter medium and evenly distributed with the normalized height 0–1; (b) one leak location (right cheek).

Data analysis

Comparison of simulation and experimental data. Simulations were conducted with combinations of 10 headforms from 5 NIOSH bivariate panel cells (3–7) and the 6 N95 FFRs. During 60 simulations, time-dependent temperature contours of the facial skin were monitored. Simulation results were validated by (1) comparing the thermal imaging pattern at the facial surface near the border of the respirator filter medium with thermal infrared images for one breathing cycle; (2) comparing temperature values for 11 points near the border of the respirator filter medium from the CFD simulation and IR thermal images at 4.2 s; (3) comparing time-dependent temperature profiles at one leak location during one breathing cycle between the simulation and thermal images; and (4) comparing leak locations for the simulation and thermal imaging results.

Time clocks were not always easy to match when comparing temperatures between thermal images and simulations. Temperature was known at only two instances in time (0.7 and 4.2 s) during thermal image videos, when nostril velocities reached the upper or lower limit, while temperature was known at all points during a simulation. In this study, temperatures were only measured at $t = 4.2$ s for 11 regions near the border of the respirator filter medium. The average temperature of 10 points (5 points on each side of the face) was obtained in each of 11 regions (Fig. 7a).

Temperature was also obtained at one leak location (right cheek) for a breathing cycle (Fig. 7b) by averaging values of 10 points at the leak location.

A comparison was made between leak sites identified in the 60 CFD simulations and from the 48 video images. In each NIOSH bivariate panel cell, there were two digital headforms (simulations) and 1–3 subjects (IR video images). Comparisons were made between each headform in the same cell. For each cell, each set of headform temperature measurements was then compared with temperature measurements for each IR video subject. At one measurement site, the number of leaks for experiments (48 subject-N95 FFR combinations) or simulations (60 headform-N95 FFR combinations) was defined as the total count of leaks at that area. The total number of leaks for four areas in Fig. 6 was obtained by adding all four areas' leak numbers. The percentage was used to compare the experimental and simulation data. The numerator is the number of leaks at one area, and the denominator was the total number of leaks in all four areas. These percentages indicated how many of the leaks, out of 100%, were located in a certain site.

Some combinations of respirator and headform were excluded due to improper matching (i.e. panel cells 3 and 4 and the medium/large N95 FFR; panel cell 7 and the small/medium N95 FFR) (Zhuang *et al.*, 2007).

Filter-to-faceseal leakage ratio

Post-processing of CFD results allowed calculation of mass flow rate at an arbitrary interface. Breathing air and ambient air are exchanged through two pathways: at the faceseal and through the filter medium (Grinshpun *et al.*, 2009). The contribution of each pathway is quantified by a 'filter-to-faceseal leakage' (FTFL) ratio as follows:

$$\mathrm{FTFL} = \frac{\text{Mass flow rate through the filter medium}}{\text{Mass flow rate through the faceseal leakage}}, \quad (4)$$

which is opposite of the 'faceseal leakage-to-filter' ratio proposed by Grinshpun *et al.* (2009), who used the particle flux instead of the mass flow rate.

A higher FTFL ratio means that there is a higher percentage of air flow passing through the filter medium than the faceseal leakage.

Sensitivity analysis

The CFD model was used to study the factors that impact the FTFL ratio by adopting different boundary conditions with the same geometries. First, simulations with three different breathing velocity profiles (normal breathing pattern and two deep breathing patterns) were conducted, while input parameters and other boundary conditions in Tables 2 and 3 did not change. The normal breathing pattern is shown in Fig. 5. The breathing velocity increases 2–3 times when the breathing pattern shifts from normal to deep (Grinshpun *et al.,* 2009). The two deep breathing patterns were achieved by scaling the base velocity profiles to two times and three times on the nostril.

Second, FTFL ratios were calculated in the simulations with different viscous resistance coefficients $1/\alpha$ of the filter medium ($1/\alpha = 5.60\times10^{9}$, 1.12×10^{10}, 5.60×10^{10}, and $1.12\times10^{11}\,\mathrm{m}^{-2}$), while boundary conditions and other input parameters in Tables 2 and 3 did not change. Finally, the freestream air flows were introduced into the CFD model. The velocity inlet boundary condition was applied at the exterior Zone III boundary (Fig. 4). Simulations were conducted with three different freestream velocities, while input parameters and other boundary conditions did not change. Their directions were all toward the human face (–z axial direction), and magnitudes were 0.1, 0.5, and 1.0 m/s with the same turbulence intensity 1.55% and length scale 100 mm, which agree with the freestream boundary condition applied by Anthony and Flynn (2006).

RESULTS

Figure 8 shows the evolution of the temperature contours from the IR video images and the simulation in one breathing cycle for a panel cell 4 headform and the 3M 8210 respirator. The shaded areas represent the filter medium covering the face. At $t = 0$ s, the facial skin had an uneven temperature distribution, the forehead and chin had the highest

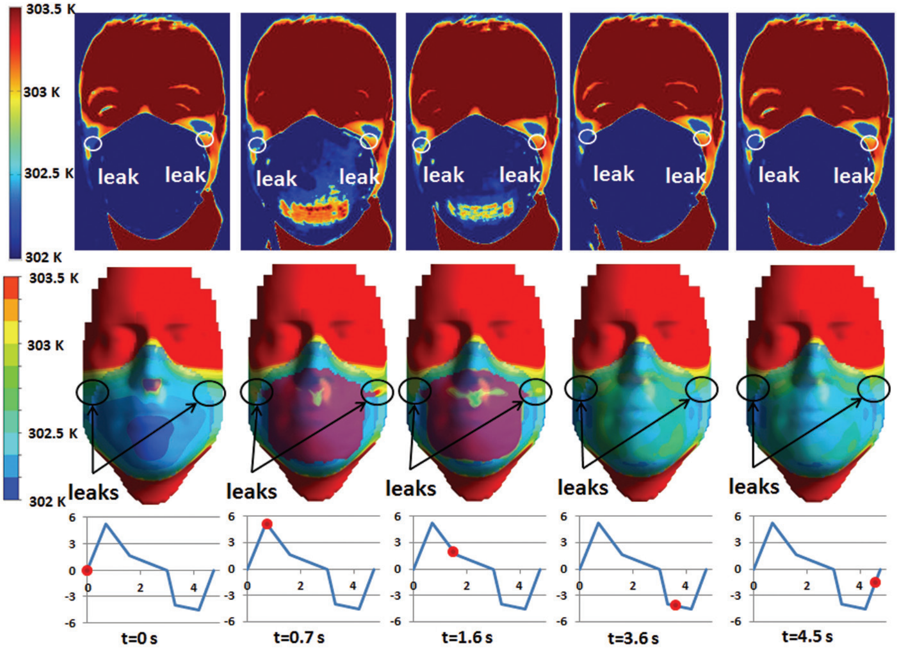

Fig. 8. Temperature contours in one breathing cycle (NIOSH bivariate panel size 4 headform and 3M 8210 FFR). The first row is the measured respiratory phase infrared colorimetric face temperature in which changes at left and right cheek regions indicated two leaks during a respirator quantitative fit test (1.5 K infrared temperature range; ambient temperature and relative humidity are 295.7 K and 18%, respectively) (Roberge *et al.,* 2011). The second row is the simulated time-dependent temperature distributions from the simulation results. The third row gives the instant breathing velocity at $t = 0$, 0.7, 1.6, 3.6, and 4.5 s.

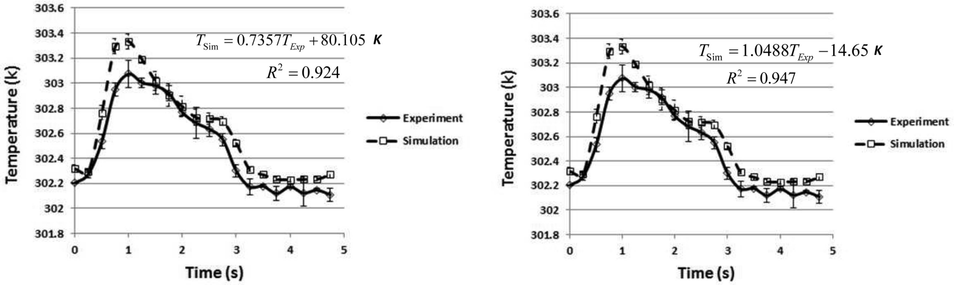

a) b)

Fig. 9. Temperatures: (a) 11 regions for inhalation at $t = 4.2$ s; (b) one leak location (right cheek) in one breathing cycle.

temperatures, and the cheek had the lowest temperature. At $t = 0.7$ s, the exhaled air velocity reached the upper bound. Because exhaled air temperature is higher than facial skin temperature, temperature increases inside the respirator, especially between the nose tip and upper lip. The region of increased temperatures expands and crossed the respirator border. At $t = 1.2$ s, the region of increased temperature shrinks as breathing velocity decreases. Temperature near the cheek bones is higher than at $t = 0$ s. At $t = 3.6$ s, the inhaled air flow velocity is close to its maximum. Temperature of inhaled air passing through the filter medium is lower than facial temperature, while inhaled air passing through faceseal leaks is at slightly less than facial temperature. At $t = 4.5$ s, the velocity at the nostril is close to zero.

During one respiration cycle, facial temperature inside the respirator changes markedly, but external to the respirator, it does not change unless there is a leak. Changes in temperature at the leak sites were easier to observe in the simulations than in thermal images with human subjects, which were impacted by head movements, light sources, respirator straps, and glasses.

Mean values and standard errors of temperatures measured at 11 locations and one leak location are shown in Fig. 9 (cell 4 headform and 3M 8210). Simulation results agree with human subject images in the nose and cheek regions. The largest difference occurs in the chin region (error is approximately 0.8 K). Linear regression analysis was carried out for $t = 4.2$ s and time-dependent profiles, and results are shown in Fig. 9.

For the four anatomical sites, 120 leaks occurred in 60 simulations, and 73 leaks were detected in the IR video images (Table 4). Because five pairs of headforms were combined with six respirators, 23 out of 30 (76.7%) combination pairs had the same leak site(s). Thus, combined with the same respirator, two headforms in the same panel cell tended to have the same leak site(s). Among 48 subject–respirator combinations, leak site(s) for 20 (42%) were identical to leak site(s) for one of the corresponding headform–respirator combinations. The leak site(s) of 39 subject–respirator combinations (83%) were covered by the leak regions for both headform–respirator combinations. More leak sites were identified in the simulations than in the subject IR images.

The IR images and simulations showed a similar fraction of leaks for each of the four leak sites (within 8%) (Table 5). For all sites combined, one-third of leaks occurred at the nose and at each check, while the chin region had about 10% of leaks. When only matched combinations were examined, the highest fraction of leaks occurred at the nose (40–50%).

With increasing breathing velocity, the FTFL ratio increased in a nonlinear manner (Fig. 10). Deep breathing patterns generated 34–62% higher FTFL ratios than normal breathing.

The FTFL ratio increased with decreasing filter viscous resistance coefficient ($1/\alpha$) (Fig. 11). There is a higher percentage of air flow passing through the filter medium than the faceseal leakage for a smaller filter viscous resistance coefficient.

CFD results with different freestream velocities showed no significant difference in the FTFL ratio (Fig. 12). At the region near the respirator's outermost surface, the magnitude of the freestream velocity dropped to $0.1 - 0.2$ m/s, which was too low to have a significant impact on the breathing air pathway. Additionally, the direction of the freestream velocity was tangent to the respirator's outermost surface, and the freestream did not directly interfere with leaking air flow. Thus, the freestream flow had limited influence on the air flow inside the respirator or at the leak regions.

Table 4. Leak locations for subject-N95 FFR combinations and headform-N95 FFR combinations (gray areas indicate unfitted combinations): area A: nasal region; area B: right cheek region; area C: left cheek region; area D: chin region.

NIOSH bivariate panel cell		3M 1860	3M 1860s	Moldex 2200	Moldex 2201	3M 8210	3M 8110
3	Subject 1	A	A	B, C	B	B, C, D	A
	Subject 2	A	A, D	A	B, C	B, C	D
	Subject 3	A, D	A, D	B, C	A	A	A
	Headform 1	A, D	A, D	B, C	A, B, C	B, C, D	A, D
	Headform 2	A, D	A, D	B, C	A	B, C, D	A, D
4	Subject 4	B, C	A, B	C	B	B, C	A
	Headform 3	A, B, C	A, B, C	B, C	B, C	B, C	A, B, C
	Headform 4	A, D	A, B, C	A	B, C	B, C	A
5	Subject 5	A	A, B	A	A, B	B, C	A
	Headform 5	A, D	A	A	B, C	B, C	A
	Headform 6	A, D	A	A	A	B, C	A
6	Subject 6	A, B, C	A, B, C	A	A	B, C	A
	Subject 7	B, C	A	A	A	B, C	A
	Headform 7	A, B, C	A, B, C	A	A	B, C	A
	Headform 8	A, B, C	A, B, C	A	A	B, C	A
7	Subject 8	C	B, C, D	A	C	B, C	B
	Headform 9	A, B, C	B, C, D	A, B, C	B, C	B, C	B, C
	Headform 10	A, B, C	B, C, D	A, B, C	B, C	B, C, D	None

Table 5. Total number of leaks at four anatomical leak sites.

Leak site	Total combinations		Matched respirator size-face combinations	
	IR images	Simulations	IR images	Simulations
Nose	28 (38%)	38 (32%)	23 (48%)	33 (40%)
Right cheek	21 (29%)	34 (28%)	13 (27%)	21 (26%)
Left cheek	22 (25%)	34 (28%)	9 (19%)	21 (26%)
Chin	6 (8%)	14 (12%)	3 (6%)	7 (9%)
Total	77	120	48	82

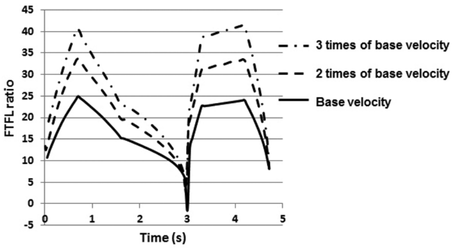

Fig. 10. FTFL ratios calculated in the simulations with different breathing velocities: the base velocity (normal breathing), and two and three times of the base velocity (deep breathing).

DISCUSSION

In one study, Oestenstad *et al.* (1990) found that leaks at the nose, cheek, and chin accounted for 53, 14, and 34% of total leaks, respectively.

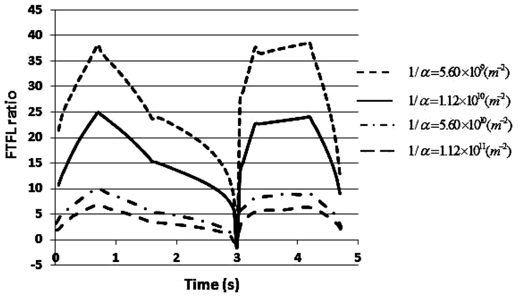

Fig. 11. FTFL ratios calculated in the simulations with different viscous resistance coefficients $1/\alpha$ of FFR filter medium.

A more recent study showed more leaks at the cheek (40%) and fewer at the nose (37%) and chin (23%) (Oestenstad *et al.,* 2010). Neither of these matches the trends noted in this study for either CFD simulations or IR images from human subjects, where the nose was generally the most common and the chin the least common leak site.

This may be due to differences in subjects, respirators, and methods used to identify leak sites. In Oestenstad *et al.* (2010), face width ranged from 115 to 147 mm and face length ranged from 105 to 130 mm, while the range of each dimension was less in this study (face width = 126–147 mm; face length = 111–126 mm). Oestenstad *et al.* (2010) used

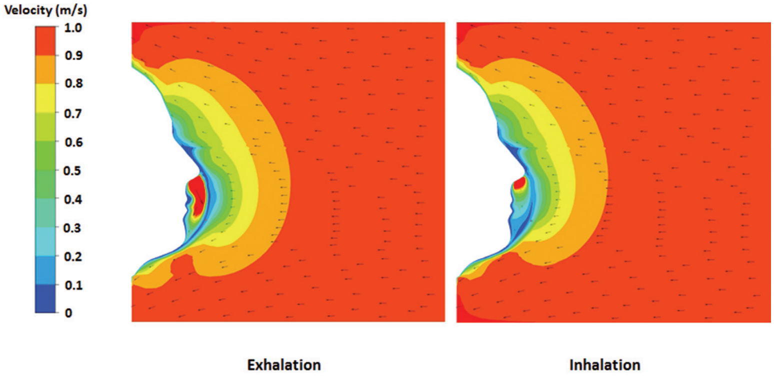

Fig. 12. The velocity contour and vector field on the sagittal plane from the simulation with freestream velocity 1 m/s .

AO 5-Star Series, North 7700 Series, and Survivair Series 2000; all of which are elastomeric respirators that are likely to fit somewhat differently than FFRs.

There are several limitations for the proposed CFD method. The first limitation is that the experimental study used human test subjects whose exact facial dimensions are different from the headforms used in the computational study. Even though the subjects were classified into five sizes based on the NIOSH bivariate respirator fit test panel, the impact of their differences on the leakage of the FFR is unknown. The second limitation of the proposed CFD approach is that only 10 sizes of headforms and 6 models of the FFR were included in this study; therefore, we cannot comment on other models. Future work will include constructing enough FE headforms that can adequately represent US respirator users. The third limitation is the costly Central Processing Unit computation time. A contact simulation requires approximately 2 h to set up and 1 h to run, and a CFD simulation requires approximately 1 h to set up and 6 h to run (Intel Xeon CPU X5660 2 processors 2.80X2 GHz, RAM 24.0 GB). To reduce computation time, future work will also include writing a program that can automatically set up the contact and CFD simulations and invoke commercial solvers to calculate results. If FE headforms are pre-constructed, the time for setting up simulations would drop significantly. If high-performance computers are introduced, the time for running simulations would not be an issue.

In this study, we made the following assumptions: (i) nasal breathing only; (ii) considering only conduction and convection for the heat transfer problem as radiation, and water evaporation were ignored; (iii) the ear and the back of head did not affect the breathing air flow; (iv) no FFR variations; (v) no head movement; and (vi) no respirator deformation during the CFD simulation. Potential error sources contributing to discrepancies between simulation and experiment include possible contributions from the above-mentioned assumptions, the difference between the subjects' faces and the headform models, numerical errors, and experimental errors. Other validation methods will also be investigated in future work because the IR method is still in its infancy stage with regard to FFR studies. Future work will introduce a particle movement model into CFD simulations, which could potentially allow for predicting respirator fit factors (Hinds and Kraske, 1987; Holton *et al.,* 1987; Liu *et al.,* 1993; Crutchfield *et al.,* 1994; Bryant and Mensch, 2011).

SUPPLEMENTARY DATA

Supplementary data can be found at http://annhyg.oxfordjournals.org/.

FUNDING

National Institute for Occupational Safety and Health projects (Contract # 254-2009-M-31878 and 254-2010-M-36735).

Acknowledgements—The authors appreciate the anonymous reviewers for their constructive comments and suggestions to improve the quality of this paper.

Disclaimer—The findings and conclusions in this paper are those of the authors and do not necessarily represent the views of the National Institute for Occupational Safety and Health.

REFERENCES

ANSYS. (2009) ANSYS FLUENT 12.0 User's Guide. Canonsburg: ANSYS Inc.

Anthony TR, Flynn MR. (2006) CFD model for a 3-D inhaling mannequin: verification and validation. Ann Occup Hyg; 50: 157–73.

Anthony TR, Flynn MR, Eisner A. (2005) Evaluation of facial features on particle inhalation. Ann Occup Hyg; 49: 179–93.

Bryant RA, Mensch A. (2011) Characterizing inward leakage in a pressure-demand, self-contained breathing apparatus. J Occup Environ Hyg; 8: 437–46.

Butler KM. (2008) A computational model of an outward leak from a closed-circuit breathing device, J Int Soc Resp Prot; 25: 53-65.

Chung TJ. (2001) Computational fluid dynamics. Cambridge: Cambridge University Press.

Craven BA, Settles GS. (2006) A computational and experimental investigation of the human thermal plume. J Fluids Eng, 128: 1251.

Crutchfield CD, Park DL. (1997) Effect of leak location on measured respirator fit. Am Ind Hyg Assoc J; 58: 413–7.

Crutchfield CD, Ruiz A, Van Ert M. (1994) A validation study of respirator fit testing by controlled negative pressure. Appl Occ Environ Hyg; 9: 362–6.

De Greef S, Claes P, Vandermeulen D *et al.* (2006) Large-scale in-vivo Caucasian facial soft tissue thickness database for craniofacial reconstruction. Forensic Sci Int; 159: S126–46.

Dubrowski KM. (1975) Studies in breath-alcohol analysis: biological factors. Z Rechtsmedizin; 78: 93–117.

Fiala D, Havenith G, Bröde P *et al.* (2012) UTCI-Fiala multi-node model of human heat transfer and temperature regulation. Int J Biometeorol; 56: 429–41.

Gao N, Niu J. (2004) CFD study on micro-environment around human body and personalized ventilation. Build Environ; 39: 795–805.

Gao P, Jaques PA, Hsiao TC *et al.* (2011) Evaluation of nano- and submicron particle penetration through ten nonwoven fabrics using a wind-driven approach. J Occup Environ Hyg; 8: 13–22.

Grinshpun SA, Haruta H, Eninger RM *et al.* (2009) Performance of an N95 filtering facepiece particulate respirator and a surgical mask during human breathing: two pathways for particle penetration. J Occup Environ Hyg; 6: 593–603.

Gupta JK, Lin CH, Chen Q. (2010) Characterizing exhaled airflow from breathing and talking. Indoor Air; 20: 31–9.

Han D, Lee J. (2005) Evaluation of particulate respirators using inward leakage (IL) or total inward leakage (TIL) testing-Korean experience. Ann Occup Hyg; 49: 569–74.

Harber P, Beck J, Luo J. (1997) Study of respirator effect on nasal-oral flow partition. Am J Ind Med; 32: 408–12.

Hayashi T, Ishizu Y, Kato S *et al.* (2002) CFD analysis on characteristics of contaminated indoor air ventilation and its application in the evaluation of the effects of contaminant inhalation by a human occupant. Build Environ; 37: 219–30.

Hinds WC, Kraske G. (1987) Performance of dust respirators with facial seal leaks: I. Experimental. Am Ind Hyg Assoc J; 48: 836–41.

Holton PM, Tackett DL, Willeke K. (1987) Particle size-dependent leakage and losses of aerosols in respirators. Am Ind Hyg Assoc J; 48: 848–54.

Hyun S, Kleinstreuer C. (2001) Numerical simulation of mixed convection heat and mass transfer in a human inhalation test chamber. Int J Heat Mass Transfer; 44: 2247–60.

Jones AW. (1982) Quantitative measurements of the alcohol concentration and the temperature of breath during a prolonged exhalation. Acta Physiol Scand; 114: 407–12.

Lee SA, Grinshpun SA, Adhikari A *et al.* (2005) Laboratory and field evaluation of a new personal sampling system for assessing the protection provided by the N95 filtering facepiece respirators against particles. Ann Occup Hyg; 49: 245–57.

Lei Z, Yang J, Zhuang Z. (2010) Contact pressure study of n95 filtering facepiece respirators using finite element method. CAD Applications; 7: 847–61.

Lei Z, Yang J, Zhuang Z. (2011) Human face and N95 filtering facepiece respirator interaction: contact pressure simulation and validation. J Occup Environ Hyg; 29: 46–58.

Li Y, Wong T, Chung J *et al.* (2006) In vivo protective performance of N95 respirator and surgical facemask. Am J Ind Med; 49: 1056–65.

Liu B, Lee J, Mullins H *et al.* (1993) Respirator leak detection by ultrafine aerosols: a predictive model and experimental study. Aerosol Sci Tech; 19: 15–26.

Ng EY, Tan HM, Ooi EH. (2010) Prediction and parametric analysis of thermal profiles within heated human skin using the boundary element method. Philos Transact A Math Phys Eng Sci; 368: 655–78.

Oestenstad RK, Bartolucci AA. (2010) Factors affecting the location and shape of face seal leak sites on half-mask respirators. J Occup Environ Hyg; 7: 332–41.

Oestenstad RK, Dillion HK, Perkins LL. (1990) Distribution of faceseal leak sites on a half-mask respirator and their association with facial dimensions. Am Ind Hyg Assoc J; 51: 285–90.

Pennes HH. (1948) Analysis of tissue and arterial blood temperatures in the resting human forearm. J Appl Physiol; 1: 93–122.

Pope SB. (2000) Turbulent flows. 1st edn. Cambridge: Cambridge University Press.

Posner JD, Buchanan CR, Dunn-Rankin JD. (2003) Measurement and prediction of indoor air flow in a model room. Energ Buildings; 35: 515–26.

Roache PJ. (1998) Verification and validation in computational science and engineering. Albuquerque: Hermosa Publishers.

Roberge RJ, Monaghan WD, Palmiero AJ *et al.* (2011) Infrared imaging for leak detection of N95 filtering facepiece respirators: a pilot study. Am J Ind Med; 54: 628–36.

Russo JS, Khalifa E. (2011) Computational study of breathing method for inhalation exposure. HVAC&R Res; 17: 419–31.

Sorensen DN, Voigt LK. (2003) Modeling flow and heat transfer around a seated human body by computational fluid dynamics. Build Environ; 38: 753–62.

Stern F, Wilson RV, Coleman HW *et al.* (2001) Comprehensive approach to verification and validation of CFD simulations - Part 1: methodology and procedures. J Fluids Eng; 123: 793–802.

Topping BHV, Muylle J, Ivanyi P *et al.* (2004) Finite element mesh generation. Stirling: Saxe-Coburg Publications.

Viscusi DJ, Bergman MS, Novak DA *et al.* (2011) Impact of three biological decontamination methods on filtering facepiece respirator fit, odor, comfort, and donning ease. J Occup Environ Hyg; 8: 426–36.

Yakhot V, Orszag SA. (1986) Renormalization-group analysis of turbulence. I. Basic theory. J Sci Comput; 1: 3.

Zhuang Z, Bradtmiller B. (2005) Head-and-face anthropometric survey of U.S. respirator users. J Occup Environ Hyg; 2: 567–76.

Zhuang Z, Bradtmiller B, Shaffer RE. (2007) New respirator fit test panels representing the current U.S. civilian work force. J Occup Environ Hyg; 4: 647–59.

Zhuang Z, Benson S, Viscusi D. (2010) Digital 3-D headforms with facial features representative of the current US workforce. Ergonomics; 53: 661–71.

APPENDIX 1

For an arbitrary node i on the oxy plane and a surface S, the distance function $\mathrm{Dist}(\mathbf{v}_i, S)$ is defined as follows:

(1) if the projection of i along the z axial direction intersects with the surface S at a point j,

$$\mathrm{Dist}(\mathbf{v}_i, S) = \mathbf{v}_j - \mathbf{v}_i \,, \tag{A1}$$

where $\mathbf{v}_i$ is the position vector of i, and $\mathbf{v}_j$ is the position vector of the point j;

(2) if the projection of i along the z axial direction does not intersect with the surface S,

$$\mathrm{Dist}(\mathbf{v}_i, S) = [0,0,0]^T \,. \tag{A2}$$

There are five steps to calculate $\mathrm{Dist}(\mathbf{v}_i, S)$.

Step 1: Project the surface S along the z axial direction on the oxy plane to obtain a new surface $S^{'}$ and find a vertex k of $S^{'}$, which has the shortest distance to i among all vertices of $S^{'}$.

Step 2: Find triangles that share the vertex k. If the intersection point j exists, i should fall in one of these triangles.

Step 3: Find a triangle $T^{'}$ which contains i and is the projection of the triangle T of surface S, as shown in Fig. A1. Because the x- and y-coordinates of j are equal to the ones of i, the problem of determining whether j lies inside T is equal to determining whether i lies inside $T^{'}$. Because the coordinates of three vertices of T are known, the positions of $T^{'}$ on the oxy plane are known. We can use the method described by Topping et al. (2004) to determine whether a point lies inside a triangle. If three triangles ($\triangle iT_1^{'}T_2^{'}$, $\triangle iT_2^{'}T_3^{'}$, and $\triangle iT_3^{'}T_1^{'}$), constructed by i and any two vertices of $T^{'}$ (in counter clockwise order) are all in counter-clockwise order, i lies inside $T^{'}$. If a triangle $\triangle ABC$ is in the counter clockwise direction,

$$\begin{vmatrix} x_A & y_A & 1 \\ x_B & y_B & 1 \\ x_C & y_C & 1 \end{vmatrix} < 0 \,, \tag{A3}$$

where x and y represent the x- and y-coordinates.

Step 4: Calculate $\mathbf{v}_j$ by solving the equation,

$$(\mathbf{v}_j - \mathbf{v}_{T1}) \bullet [(\mathbf{v}_{T1} - \mathbf{v}_{T2}) \times (\mathbf{v}_{T1} - \mathbf{v}_{T3})] = 0 \,, \tag{A4}$$

where $\mathbf{v}_{T1}$, $\mathbf{v}_{T2}$, and $\mathbf{v}_{T3}$ are the position vectors of nodes T_1, T_2, and T_3.

Step 5: Obtain the distance function by applying $\mathbf{v}_j$ to equation (1).

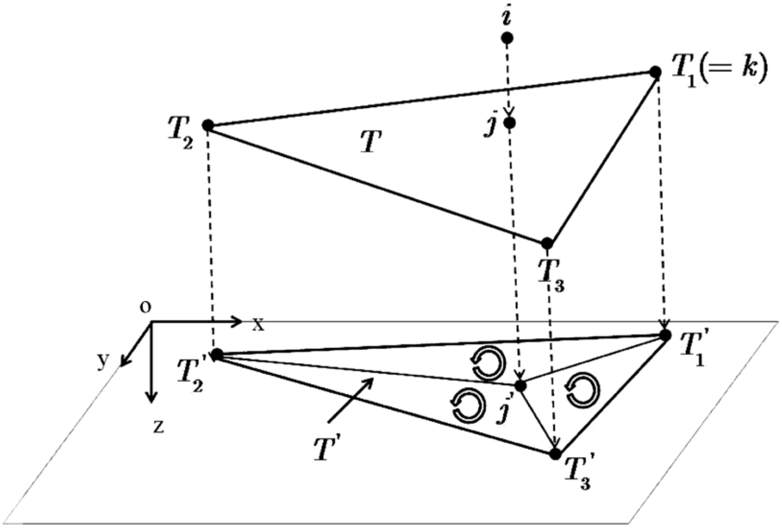

Fig. A1. Node j is the projection of the headform node i onto an FFR element T along the z axial direction, and triangle $T^{'}$ is the projection of T onto the oxy plane.

APPENDIX 2

GRID INDEPENDENCY

To access the grid independency of simulation results, three different mesh densities were created. For a size 5 headform-3M 8210 FFR simulation, the fine grid model has 1 295 910 pentahedrons, the medium grid model has 589 050 pentahedrons, and the coarse grid model has 267 750 pentahedrons. We used the grid convergence method (GCI), which is based on the Richardson extrapolation (RE) method, to estimate discretization error (Roache, 1998; Stern et al., 2001). A brief description of the GCI method is provided. A representative grid size h was defined as:

$$h = \sqrt[3]{\frac{V}{N}}, \tag{A5}$$

where V is the volume of the model, and N is the number of the solid elements. The representative grid sizes h1–3 of the fine, medium, and coarse meshes had values 3.075, 4.00, and 5.21 mm. The parameter refinement ratios were calculated as $r_{21} = h_2 / h_1 \approx 1.3$ and $r_{32} = h_3 / h_2 \approx 1.3$. Because these two parameter refinement ratios were nearly the same, the apparent order p of the method was calculated as

$$p = \frac{\left| \ln \left| \frac{f_3 - f_2}{f_2 - f_1} \right| \right|}{\ln(r_{21})}, \tag{A6}$$

where f_{1-3} are the solutions of the three mesh densities. With the apparent order p, we got the extrapolated values using the equation

$$f_{\mathrm{exact}}^{21} = (r_{21}^{p} f_1 - f_2) / (r_{21}^{p} - 1). \tag{A7}$$

The approximate relative error, extrapolated relative error, and fine grid convergence index were obtained respectively from

$$e_a^{21} = \left| \frac{f_1 - f_2}{f_1} \right| \tag{A8}$$

$$e_{\mathrm{exact}}^{21} = \left| \frac{f_{\mathrm{exact}}^{21} - f_1}{f_{\mathrm{exact}}} \right| \tag{A9}$$

$$GCI_{\mathrm{fine}} = 1.25 \frac{e_a^{21}}{r_{21}^{p} - 1}. \qquad \text{(A10).}$$

Simulation solutions at two locations were probed as shown in Fig. A2. The leak location (right cheek) is a point on the facial skin surface, and the center line of the FFR filter medium outward surface is a

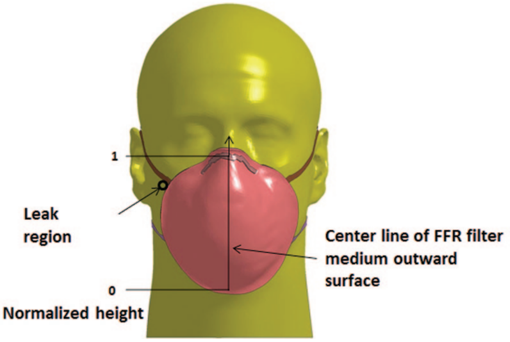

Fig. A2. Two locations where solutions were measured and evaluated.

Table A1. Summary of RE at the leak location.

	Exhalation				Inhalation			
	p	e_a^{21}	e_{exact}^{21}	$\mathrm{GCI}_{\mathrm{fine}}$	p	e_a^{21}	e_{exact}^{21}	$\mathrm{GCI}_{\mathrm{fine}}$
T	1.2	0.20%	0.55%	0.69%	0.6	0.45%	2.57%	3.30%
P	1.6	0.27%	0.51%	0.64%	2.7	0.59%	0.57%	0.71%
u_1	1.2	0.52%	1.39%	1.77%	3.7	0.90%	0.54%	0.68%
u_2	3.3	1.61%	1.18%	1.46%	4.0	0.44%	0.24%	0.29%
u_3	2.7	30.66%	22.93%	37.18%	1.6	2.10%	3.87%	5.03%
k	4.3	0.76%	0.36%	0.45%	3.2	1.02%	0.78%	0.97%
ε	1.5	0.56%	1.18%	1.46%	0.6	0.84%	5.17%	6.14%

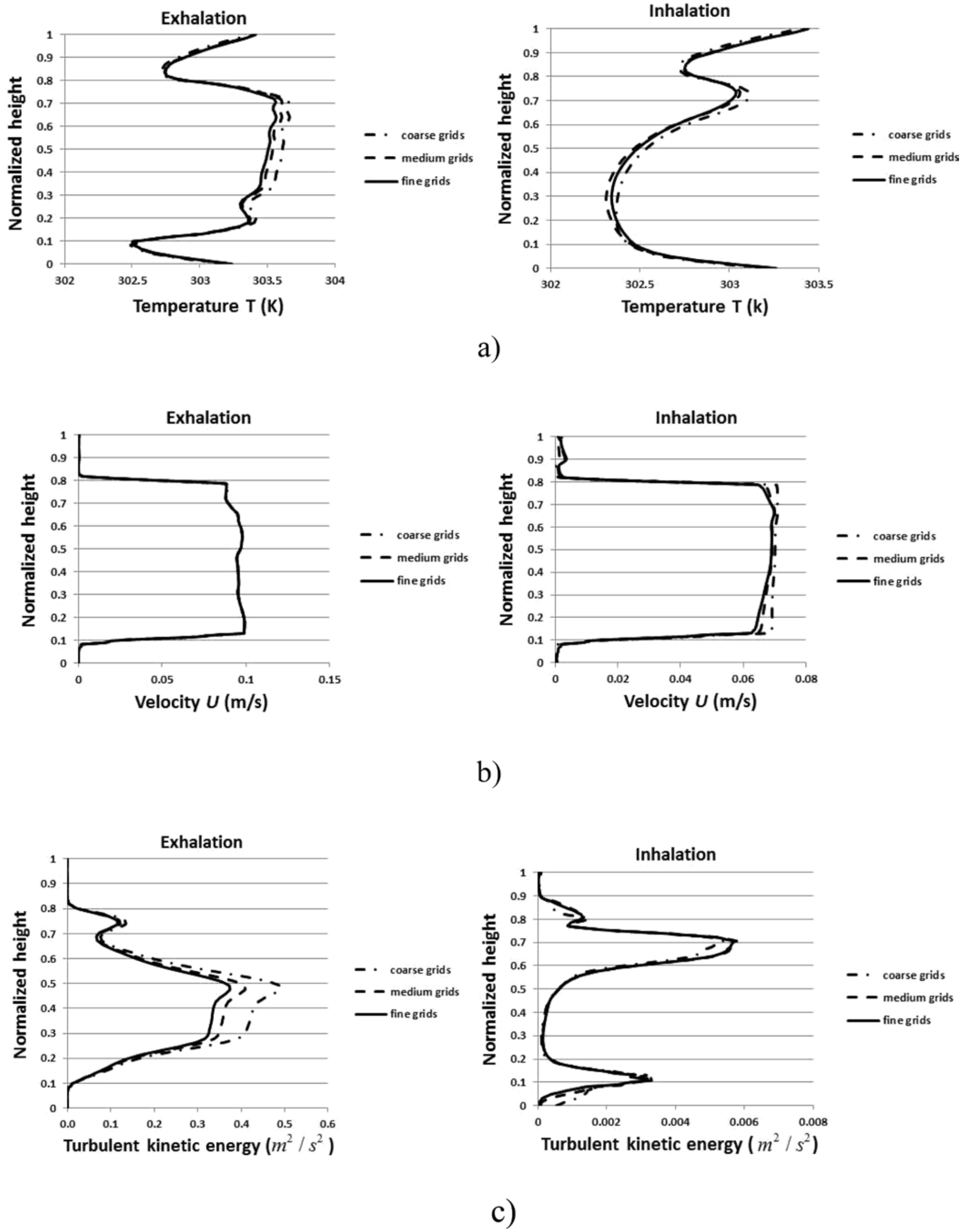

Fig. A3. (a) Temperature, (b) velocity, and (c) turbulent kinetic energy at the center line of FFR filter medium outward surface with three grid resolutions.

series of points (about 50) on the sagittal plane. The height of the center line is normalized in such way that the height 0 indicates the bottom of the FFR filter medium, and the height 1 indicates the top of the FFR filter medium. By measuring the solutions of the temperature T, pressure P, velocities u_{1-3}, kinematic energy k, and turbulence Eddy dissipation ε at the two locations, p, e_a^{21}, e_{exact}^{21}, and GCI_{fine} were calculated from equations A5–10. Table A1 gives the summary of RE at the leak location. The

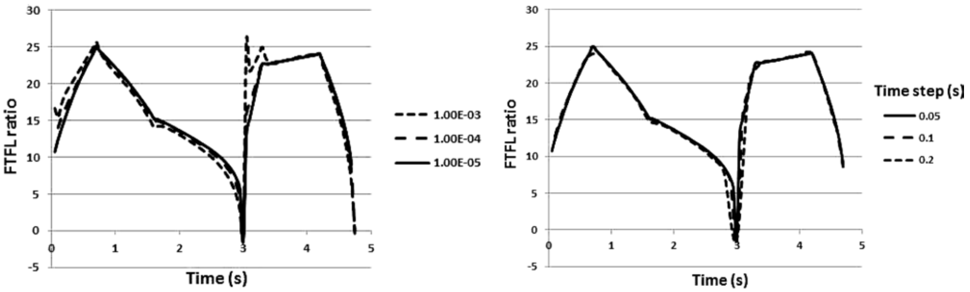

a) b)

Fig. A4. Time-dependent profiles of FTFL ratio with (a) different iteration stop criteria and (b) time step sizes.

apparent order *p* was 0.4–4.3, consistent with the arranged numerical schemes. The GCI of the solutions were low (<7%), despite the GCI of u_3 during exhalation (37.18%). The large GCI of u_3 may come from the very small magnitude of u_3 during exhalation. Figure A3 presents temperatures, *U* velocities, and turbulent kinetic energies at the center line of the FFR filter medium outward surface with three grid resolutions. Differences distinctly appeared at the region of the normalized height 0.15–0.7, where most of the air flow streamlines passed through the FFR filter medium. The increasing magnitudes of solutions caused the differences in simulations with three grid resolutions. The apparent order *p* at the region of normalized height 0.15–0.7 was 1.0–4.0, and the highest GCI was 8.53%. In general, small differences in temperatures, velocities, and turbulence kinetic energies between the middle and fine meshes indicated good mesh independence. Because the middle mesh required much less calculating time than the fine mesh did, the middle mesh was used in all simulations.

ITERATION ERRORS

Because the continuity residual had the slowest convergent speed, it was selected as the iteration stopping criterion. When the continuity residual reached the assigned limit, the iteration stopped and moved the calculation to the next time step. We ran three simulations with limits of 1.00E-3, 1.00E-4, and 1.00E-5. The time-dependent profiles of the FTFL ratio were shown in Fig. A4a. The profile of the simulation with the limit of 1.00E-3 had a distinct oscillation at $t = 3.2\,\mathrm{s}$, while the profiles with the limit of 1.00E-4 and 1.00E-5 agreed with each other very well. Because the limit of 1.00E-4 required much less calculating time than the limit of 1.00E-5 did, the iteration stopping criterion was set as 1.00E-4. It was observed that, after the continuity residual reached 1.00E-4, other variables' residuals were all between 1.00E-4 and 1.00E-8.

TIME STEP ERRORS

Simulations with different time step sizes (0.01, 0.025, 0.05, 0.1, and 0.2 s) were conducted, and the time-dependent profiles of the FTFL ratio were plotted. The results had apparent time step error only in the simulation with time step size 0.2. Figure A4b shows the comparison of the FTFL ratio with the time step sizes 0.05, 0.1, and 0.2 s. The results with the time step sizes 0.05 and 0.01 s had good agreement. Thus, the time step size 0.05 s was selected for all other simulations.